AIAA JOURNAL
Vol. 43, No. 4, April 2005

Stability of Hypersonic Boundary Layers over a Compression Corner

P. Balakumar*
NASA Langley Research Center, Hampton, Virginia 23681
Hongwu Zhao†
Old Dominion University, Norfolk, Virginia 23529
and
Harold Atkins‡
NASA Langley Research Center, Hampton, Virginia 23681

The stability of hypersonic boundary layers over a compression corner is investigated numerically. To compute the shock and the interaction of the shock with the instability waves, the simulation solves the three-dimensional Navier–Stokes equations using a high-order, weighted, essentially nonoscillatory shock-capturing scheme. After computing the mean flowfield, the procedure then superimposes two-dimensional unsteady disturbances at the inflow and computes the evolution of these disturbances in downstream direction. Because of the interaction of the shock with the boundary layer, a separation bubble forms at the corner, and two compression waves form near the separation and reattachment points. These compression waves merge farther away from the boundary layer to form a shock. The investigation of the evolution of the second mode shows three distinct regions. One is upstream of the separation bubble where the disturbances grow in agreement with the linear theory of similarity boundary layers. The second region is the separation bubble region where the disturbances remain neutral. These disturbances reside above the separation bubble and do not penetrate the separated region. The third region is downstream of the separation bubble where the disturbances again grow exponentially as in boundary layers.

I. Introduction

THIS work numerically investigates the stability and transition of hypersonic boundary layers over compression corners. When a large adverse pressure gradient exists in the inviscid pressure distribution, the viscous effects become important. The interaction between the oncoming boundary layer and the adverse pressure gradient drastically modifies the inviscid pressure distribution and the flowfield. Multiple shocks, flow separation, transition to turbulence, unsteadiness, and three-dimensionality appear near the interaction region. This phenomenon appears in transonic flows over airfoils, supersonic flows over compression corners, and flows over steps.

Ackert et al.[1] were the first to investigate experimentally the mutual influences of the compression shocks and the boundary layers at transonic and low supersonic Mach numbers in laminar and turbulent flow regimes. Since then, several experiments, analyses, and computations[2–7] have been performed to investigate the shock boundary-layer interactions in detail. Most of the experiments measured or computed aerodynamic quantities such as pressure distribution, skin friction, and heat-transfer rates. The measurements and the observations for laminar boundary layers showed formation of a λ shock at Mach numbers in the range of 1.2 and showed formation of multiple shocks with decreasing Mach numbers. The λ shock consists of a main shock with a preceding oblique compression wave. The flow separates in front of the main shock with a gradual increase of pressure starting upstream of the separation point. This gradual increase in pressure ends with a sharp increase near the main shock, and the flow becomes turbulent behind the shock. For turbulent flows, the measurements and observations showed formation of only normal shocks. In both cases the boundary-layer thickness increases considerably, about 10 times in laminar flows and about four times in turbulent flows.

Chapman et al.[8] conducted an extensive investigation on flow separation with steps, bases, compression corners, and curved surfaces at different Mach numbers, ranging from 0.4 to 3.6, and at different Reynolds numbers. They observed that the pressure distribution in separated flows depends on the location of the transition point relative to the reattachment and separation points. In laminar separations, the pressure initially rises smoothly, reaches a plateau and, depending on the downstream condition, rises to the final pressure smoothly. In transitional separated flows where the flow starts to become turbulent between the separation and reattachment points, the pressure initially rises smoothly, as in laminar flows, and then increases sharply near the transition region. The pressure distribution also becomes unsteady in this case. In turbulent separated flows, the pressure rise is steep from the start to the end. They also observed that the mixing layer above the separation bubble is stable in supersonic flows, and the stability increases with increasing Mach numbers. Therefore, laminar separated flows become very important in hypersonic boundary layers.

The mechanism for the upstream propagation of the disturbances in a boundary layer and in a supersonic freestream from the adverse-pressure-gradient region was first explained by Lighthill[9,10] using self-induced separation theory and later using asymptotic triple-deck theory by Stewartson and Williams.[11] The mechanism is that the separated region near the shock produces an adverse pressure gradient in the outer part of the boundary layer, and this induces further growth of the separated region until they come to an equilibrium state further upstream of the original discontinuity. This theory predicts the initial pressure rise close to the separation point, and the agreement between the calculated and the experimental pressure distribution close to the separation point is excellent.

Presented as Paper 2002-2848 at the AIAA 32nd Fluid Dynamics Conference, St. Louis, MO, 24–26 June 2002; received 30 June 2003; revision received 8 September 2004; accepted for publication 20 October 2004.

*Aerospace Engineer, Flow Physics and Control Branch, MS 170. Member AIAA.
†Graduate Research Assistant, Department of Aerospace Engineering. Member AIAA.
‡Aerospace Engineer, Computational Modeling and Simulation Branch, MS 128. Member AIAA.

Berry et al.[12] have performed detail flow visualization and phosphor thermography investigations of aeroheating and boundary-layer transition characteristics for the 0.333-scale Hyper-X forebody in the NASA LaRC 20-Inch Mach 6 air tunnel. The windward side of the model consists of three ramps, which are inclined at 2.5, 8, and 11 deg. The first ramp ends at 12.433 in. (31.58 cm), the second ramp ends at 17.767 in. (45.13 cm), and the third ramp extends up to the end of the model, which is a total of 28 in. (71.12 cm) long. The main focus of the investigation was to determine the effects of different trips on transition. They have tested several trip configurations at different angles of attack and freestream Reynolds numbers. They found, for the baseline case, without tripping at an angle of attack of 2 deg that as the unit Reynolds number is increased to 2.2×10^6/ft the transition starts to appear close to the end of the model. Doubling the Reynolds number to 4.4×10^6/ft moved the onset of transition close to the second corner and tripling the Reynolds number to 6.7×10^6/ft moved the onset between the first and the second corner.

The boundary layer over a compression corner can be divided into four regions: 1) the boundary layer before the separation, 2) the mixing layer above the separation bubble in the corner, 3) the separation bubble in the corner, and 4) the boundary layer downstream of the separation bubble. Hence, the transition to turbulence can occur because of different instabilities that can exist in these regions. In hypersonic boundary layers, the high-frequency two-dimensional second-mode-type disturbances[13] dominate the transition. Consequently, in the upstream and downstream boundary layers the transition can occur as a result of this instability. Because the streamlines are curved in the corner region, the three-dimensional disturbances can grow as a result of Görtler instability in this region. This paper will investigate the evolution of two-dimensional second-mode disturbances. Obviously, the stability and the transition depend on the flow parameters, such as Mach number, Reynolds number, the wedge angle, and the wall boundary conditions. Parameters are selected to model the Hyper-X wind-tunnel model and the experimental conditions.[12] For simplicity, the computations are performed from the downstream of the leading edge to the second corner. The compression corner has a small wedge angle of 5.5 deg. The freestream Mach number is $M = 5.373$, and the Reynolds number is $Re = 5.464 \times 10^6$/ft. These conditions simulate the experimental freestream conditions of $M = 6$ and $Re = 4.40 \times 10^6$/ft for which the onset of transition occurred close to the second corner (test 6755 run 5 in Ref. 12).

The numerical simulations are computed by solving the three-dimensional Navier–Stokes (N-S) equations using a high-order, weighted, essentially nonoscillatory (WENO), shock-capturing scheme. The code has been validated extensively against linear stability and parabolized stability computations (PSE).[14] The numerical procedure is first to compute the steady mean flowfield over the compression corner. The next step is to perform local parallel linear stability computations for this mean flow. Even though the linear stability theory is valid in slowly varying shear flows, it is performed in this complex flow to understand the stability properties of this flow and to obtain necessary parameters for further analysis and simulations. The last step is to superimpose unsteady disturbances at the inflow and to simulate the evolution of these disturbances downstream. The first section presents the governing equations, and this is followed by a brief description of the numerical method used to solve the N-S equations. The next section gives the results including mean flow computations, linear stability computations, and direct numerical simulations. The last section is a discussion with conclusions.

II. Governing Equations

The equations solved are the three-dimensional unsteady compressible N-S equations in conservation form:

$$\frac{\partial}{\partial t} Q_i + \frac{\partial}{\partial x_j}(F_{ji} - F_{vji}) = 0 \tag{1}$$

Here

$$Q_i = \begin{Bmatrix} \rho \\ \rho E \\ \rho u \\ \rho v \\ \rho w \end{Bmatrix}, \qquad [F_{ji}] = \begin{Bmatrix} \rho u_j \\ (\rho E + p)u_j \\ \rho u u_j + \delta_{1j} p \\ \rho v u_j + \delta_{2j} p \\ \rho w u_j + \delta_{3j} p \end{Bmatrix}$$

$$[F_{vij}] = \begin{Bmatrix} 0 \\ u\tau_{1j} + v\tau_{2j} + w\tau_{3j} - q_j \\ \tau_{1j} \\ \tau_{2j} \\ \tau_{3j} \end{Bmatrix} \tag{2}$$

Here (x, y, z) are the Cartesian coordinates, (u, v, w) are the velocity components, ρ is the density, and p is the pressure. E is the total energy given by

$$E = e + [(u^2 + v^2 + w^2)/2], \qquad e = c_v T, \qquad p = \rho R T \tag{3}$$

Here e is the internal energy, and T is the temperature. The shear stress and the heat flux are given by

$$\tau_{ij} = \mu \left\{ \frac{\partial u_i}{\partial x_j} + \frac{\partial u_j}{\partial x_i} - \frac{2}{3}\delta_{ij} \frac{\partial u_k}{\partial x_k} \right\}, \qquad q_j = -k \frac{\partial T}{\partial x_j} \tag{4}$$

The viscosity μ is computed using Sutherland's law, and the coefficient of conductivity k is given in terms of the Prandtl number Pr. The variables ρ, p, T and velocity are nondimensionalized by their corresponding reference variables ρ_∞, p_∞, T_∞, and $\sqrt{RT_\infty}$, respectively. The reference value for length is computed by $\sqrt{\nu x_0 / U_\infty}$, where x_0 is the location of the beginning of the computational domain in the streamwise direction. For the computation, the equations are transformed from physical coordinate system (x, y, z) to the computational curvilinear coordinate system (ξ, η, ζ) in a conservative manner, and the governing equations become

$$\frac{\partial}{\partial t} \bar{Q}_i + \frac{\partial}{\partial x_j}(\bar{F}_{ji} - \bar{F}_{vji}) = 0 \tag{5}$$

The components of the flux in the computational domain are related to the flux in the Cartesian domain by

$$\bar{Q}_i = \frac{Q_i}{J}, \qquad [\bar{F}_{ji}] = \frac{J}{|J|}[F_{ji}], \qquad \text{where} \qquad J = \left[\frac{\partial(\xi, \eta, \zeta)}{\partial(x, y, z)} \right] \tag{6}$$

The governing equations are solved using a fifth-order-accurate WENO scheme for space discretization and using a third-order, total-variation-diminishing (TVD) Runge–Kutta scheme for time integration. These methods are suitable in flows with discontinuities or high-gradient regions. These schemes solve the governing equations discretely in a uniform structured computational domain in which flow properties are known pointwise at the grid nodes. They approximate the spatial derivatives in a given direction to a higher order at the nodes, using the neighboring nodal values in that direction, and they integrate the resulting equations in time to get the point values as a function of time. Because the spatial derivatives are independent of the coordinate directions, the method can easily add multidimensions. It is well known that approximating a discontinuous function by a higher-order (two or more) polynomial generally introduces oscillatory behavior near the discontinuity, and this oscillation increases with the order of the approximation. The essentially nonoscillatory (ENO) method and the improvement of these WENO methods are developed to keep the higher-order approximations in the smooth regions and to eliminate or suppress the oscillatory behavior near the discontinuities. They are achieved by systematically adopting or selecting the stencils based on the smoothness of the function, which is being approximated. Reference 15 explains the

WENO and the TVD methods and the formulas, and Ref. 16 gives the application of the ENO method to the N-S equations. Reference 14 describes in detail the solution method implemented in this computation.

At the outflow and at the upper boundary, high-order extrapolations are used as boundary conditions. At the wall, the simulation uses viscous conditions for the velocities and a constant temperature condition, and it computes density from the continuity equation. In the mean flow computations, the simulation prescribes the similarity boundary-layer profiles at the inflow. At the unsteady computations, it superimposes the discrete eigensolution to the mean flow solution at the inflow. The procedure is to first compute the steady mean flow by performing unsteady computations using a variable time step until the maximum residual reaches a small value $\sim 10^{-5}$. These computations use a Courant–Friedrichs–Lewy number of 0.6. The next step is to introduce unsteady disturbances at the upstream end of the computational domain and to perform time-accurate computations to investigate the evolution of these disturbances downstream. The following form of the disturbances is considered:

$$q = \varepsilon \text{Real}\{\tilde{q} e^{-i\omega t}\} \qquad \text{(two-dimensional modes)} \qquad (7)$$

Here ω is the frequency, and $\tilde{q}(\eta)$ is the normalized eigenfunction, which is obtained from PSE computations.[17] Here, ε is a parameter, which controls the initial amplitude of different modes. The computations use a small value for $\varepsilon = 10^{-4}$, and so the nonlinear effects remain negligible in the entire computational domain.

III. Results

The computations are performed for the hypersonic flow over a 5.5-deg compression corner. Table 1 gives the flow parameters, and Fig. 1 shows the dimensions of the geometry and the computational domain. The dimensions and the parameters are the same as the lower surface of the Hyper-X wind-tunnel model and the experimental conditions.[12]

The grid is generated using the analytical conformal mapping formulas. The grid stretches in the η direction close to the wall and near the critical layer region and in the ξ direction close to the downstream boundary. Calculations were performed using two grid sizes (1001×301) and (1701×301), and almost identical results were obtained in both cases. This paper presents the solutions obtained with the fine grid.

Table 1 Flow parameters for the Hyper-X wind-tunnel model

Parameter	Value
Freestream Mach number	$M_\infty = 5.373$
Freestream Reynolds number	$Re_\infty = 5.464 \times 10^6$/ft
Freestream density	$\rho_\infty = 6.0891 \times 10^{-3}$ lbm/ft^3
Freestream pressure	$p_\infty = 43.384$ lbf/ft^2
Freestream velocity	$U_\infty = 3043.86$ ft/s
Freestream temperature	$T_\infty = 133.55$ R
Freestream kinematic viscosity	$\nu_\infty = 5.5707 \times 10^{-4}$ ft^2/s
Wall temperature	$T_w = 540$ R
Prandtl number	$Pr = 0.72$
Ratio of specific heats	$\gamma = 1.4$
Nondimensional frequency	$F = 1 \times 10^{-4} = 264.7$ kHz
Nondimensional frequency	F is defined as $F = 2\pi \nu_\infty f / U_\infty^2$, where f is the frequency in hertz

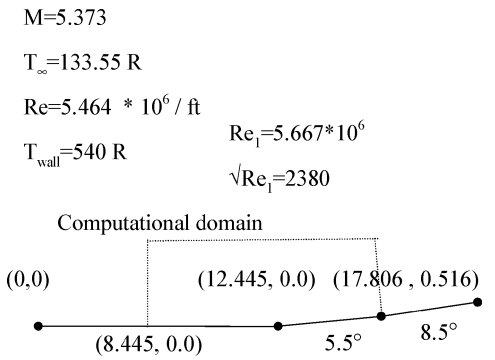

Fig. 1 Dimensions of the lower part of the Hyper-X model geometry. Dimensions are in inches.

A. Mean Flow

Figures 2–8 show the results for the steady mean flow field. Figure 2 shows the density contours, and Fig. 3 shows the streamline patterns near the corner region. Figure 4 shows the pressure distribution at the wall and at different distances from the wall $Y = 0.0$, 0.07, 0.115, and 0.225 in. Figure 5 shows the variation of the boundary-layer thickness and the displacement thickness in the axial direction.

As it is discussed earlier, the shock-boundary-layer interaction causes the boundary layer to separate near the corner and forms a separation bubble. The separation and the reattachment points are located at about 10.8 and 14.1 in., while the corner is located at 12.44 in. The boundary-layer thickness at $X = 10$ in. is about 0.08 in. Hence, the separation and reattachment points are at about a 20 boundary-layer thicknesses from the corner, and the separated region is about 40 boundary-layer thicknesses long. Figure 3 also shows that the edge of the separated region is almost a straight line and is inclined at about 3.1, while the main ramp is inclined at 5.5 deg. This new inclined surface creates two compression waves,

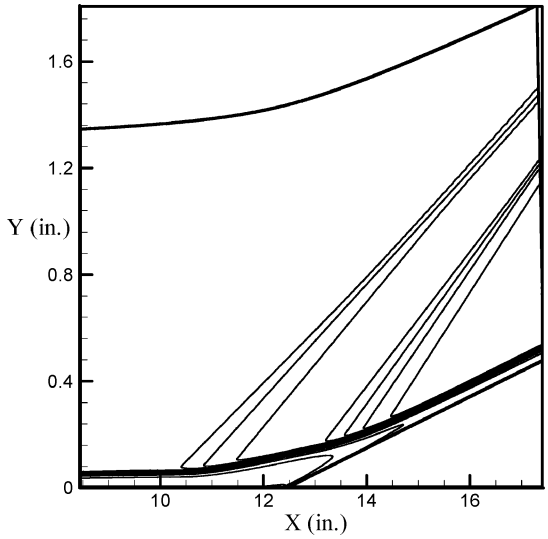

Fig. 2 Density contours for flow past a 5.5-deg compression corner.

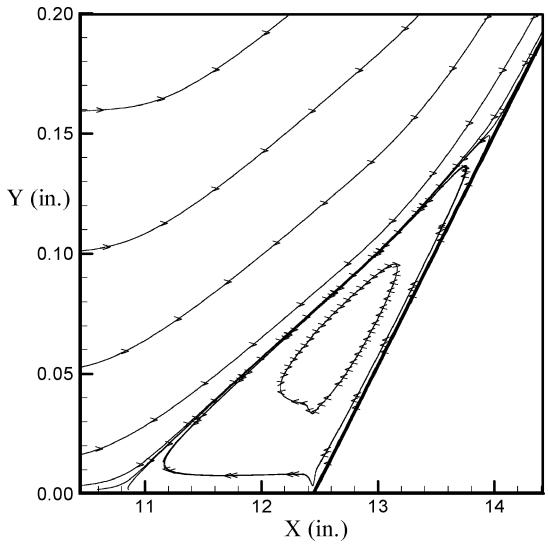

Fig. 3 Expanded view of the streamline patterns near the corner.

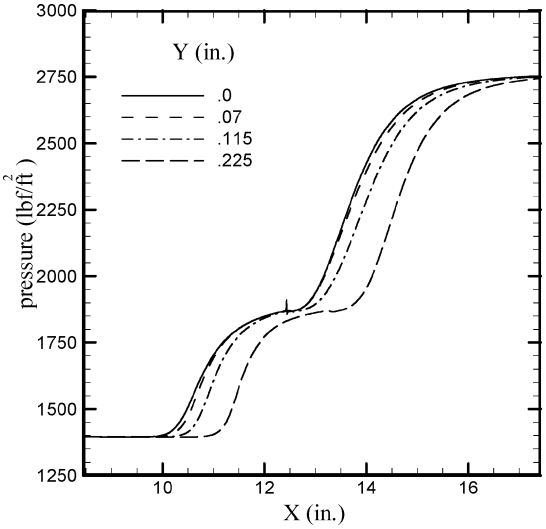

Fig. 4 Pressure distribution at different heights from the surface.

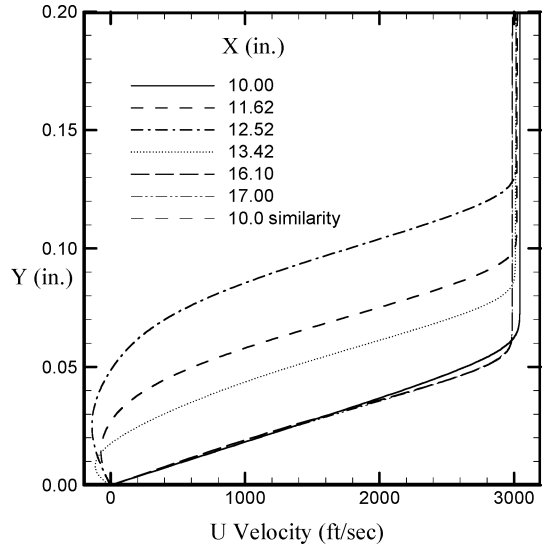

Fig. 7 *U*-velocity distributions inside the boundary layer.

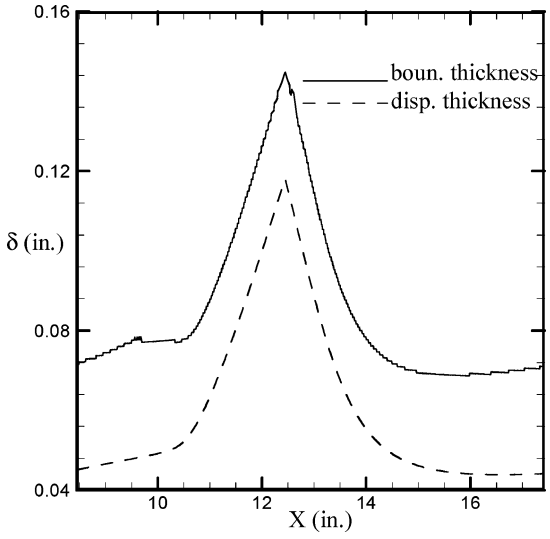

Fig. 5 Variation of the boundary layer and the displacement thickness.

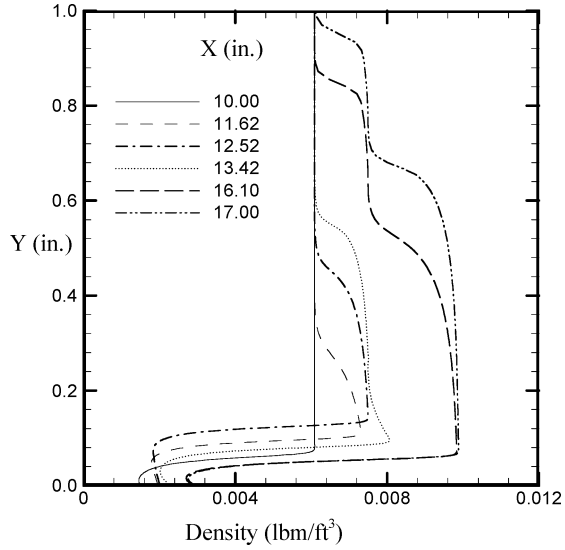

Fig. 8 Density distribution at different *X* stations.

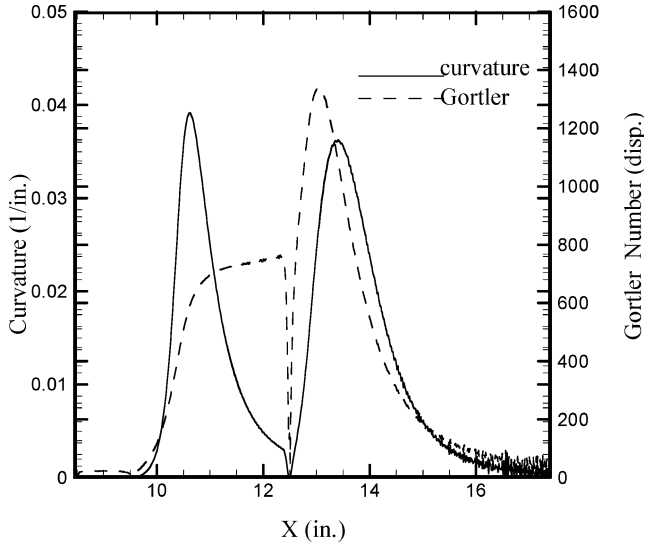

Fig. 6 Radius of the curvature and Görtler number based on displacement thickness at $Y = 0.05$ in.

one close to the separation point and another near the reattachment point, as they are seen in the density contours of Fig. 2.

The pressure distribution at the surface shows that the pressure starts to increase at $X = 10$ in., which is upstream of the separation point $X = 10.8$ in. This is the free-interaction region analyzed by Lighthill[9,10] and Stewartson and Williams.[11] The initial pressure increase saturates in the middle region and increases again. This shows that, near the corner region, the flowfield is approximately uniform. This is also evident in the density contour plot in Fig. 2. It shows that the pressure distribution at $Y = 0.0$ and 0.07 in., which are on the wall and along the edge of the boundary layer, is almost equal. This implies that the compression waves originate from outside of the boundary layer and do not penetrate inside the boundary layer. Another important observation is the growth of the boundary layer, which is depicted in Fig. 5. Initially the boundary layer grows according to the similarity profiles along a flat plate, and from about $X = 9.6$ in., the boundary-layer thickness remains constant up to the separation point $X = 10.8$ in. From the separation point, the boundary-layer thickness grows steeply as a wedge and reaches a peak value of 0.145 in. at about 12.8 in. and again decreases very steeply near the reattachment point. The boundary-layer thickness reaches a minimum value of 0.068 in. at $X = 15$ in., and this value is smaller than the boundary-layer thickness upstream of the separation. Therefore, when the hypersonic flow passes over

a compression corner, because of the compression, the boundary layer becomes smaller downstream of the separation.

Figure 6 shows the radius of curvature for a streamline located at about $Y = 0.05$ in. above the wall. This streamline approximately passes through the critical layer inside the boundary layer. The streamlines are very curved near the separation and reattachment region and have a small curvature in the middle region above the corner. To facilitate the investigation later, the Görtler number is calculated based on this curvature and the displacement thickness defined by

$$G = (U_\infty \delta_d / \nu)(\delta_d \kappa)^{\frac{1}{2}} \tag{8}$$

where δ_d is the displacement thickness and κ is the radius of curvature. The Görtler number is very high, about 800 near the separation region and about 1300 near the reattachment region. Hence, the flow can become unstable above the separation bubble as a result of Görtler instability.

Figure 7 shows the velocity profiles inside the boundary layer at different axial locations $X = 10.0$, 11.62, 12.52, 13.42, 16.10, and 17 in. The stations $X = 11.62$, 12.52, and 13.42 in. are in the separated region, and the others are outside of it. Similarly, Fig. 8 shows the density profiles across the whole domain. As observed previously, the growth and shrinking of the boundary-layer thickness are clearly seen in these figures. The maximum velocity in the recirculation region is in the order of 200 ft/s compared to 3000 ft/s at the edge of the boundary layer. The density is almost constant in the separation bubble, and the density gradient inside the boundary layer is much larger in the downstream region compared to that upstream of the corner. This figure also shows the plot of the boundary-layer profiles obtained by solving the compressible boundary-layer similarity equations. The similarity solutions should agree with the numerical solution in the region upstream of the separation point. At $X = 10.0$ in., the agreement in the velocity and the density profiles is excellent.

B. Linear Stability

After the steady mean flow is obtained, the parallel linear stability computations are performed at different streamwise stations. The velocity and density profiles normal to the wall are used as input in the stability calculations. These profiles extend from the wall to the outer computational boundary where Drichlet conditions are imposed. Figures 9a and 9b show the spatial amplification rates as a function of the nondimensional frequency F at different streamwise stations. Figure 9a shows the results at stations upstream of the corner, while Fig. 9b shows the results downstream of the corner. At $X = 8.445$ in., the results show the typical high-Mach-number two-dimensional first- and second-mode growth rate curve. The two-dimensional first mode is almost neutral, but the second mode is very unstable and has a maximum growth rate of 1.2/in. at a nondimensional frequency of $F = 0.8 \times 10^{-4}$, which corresponds to about 220 kHz. At other stations, the growth rate curves are different from that at $X = 8.445$ in. Two peaks exist: one is located in the low-frequency region near $F = 0.2 \sim 0.4 \times 10^{-4}$, and the other is located in the high-frequency region near $F = 0.7 \sim 1.0 \times 10^{-4}$. Another interesting observation is that with increasing X, the growth rate curve for a fixed X gradually shifts to the left towards the low-frequency region. At $X = 11.22$ in. the peak growth rates occur at $F = 0.4 \times 10^{-4}$ and 1.0×10^{-4}, and at $X = 12.07$ in. they occur at $F = 0.25 \times 10^{-4}$ and 0.6×10^{-4}. Similarly, Fig. 9b shows the stability results for the stations downstream of the corner. Again at $X = 16.10$ in., which is farther downstream from the separation region, the high-Mach-number stability results are obtained. At other stations, which are in the separation region, the same growth rate curves with two peaks are seen. In this region, with increasing X, the growth rate curves shift to the right toward the high-frequency region.

Because transition is caused by the cumulative growth of unstable disturbances, the variation of the growth rate in the X direction is computed for a fixed frequency. Figure 10 shows the results for $F = 0.80$, 0.25, and 0.35×10^{-4}. The first observation is that the

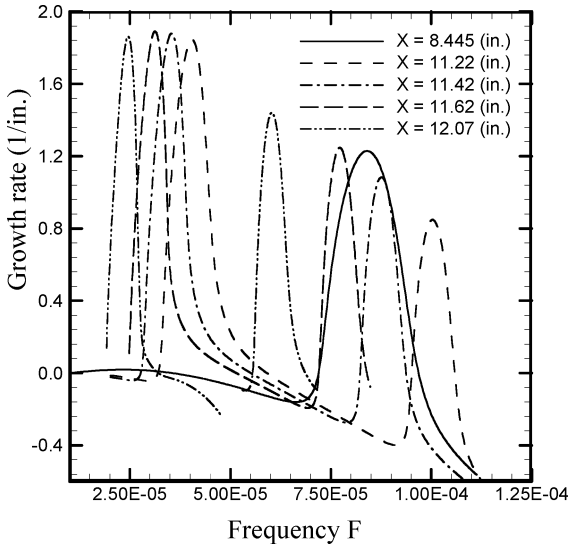

Fig. 9a Growth rate from linear stability computations at different X stations (upstream of the corner).

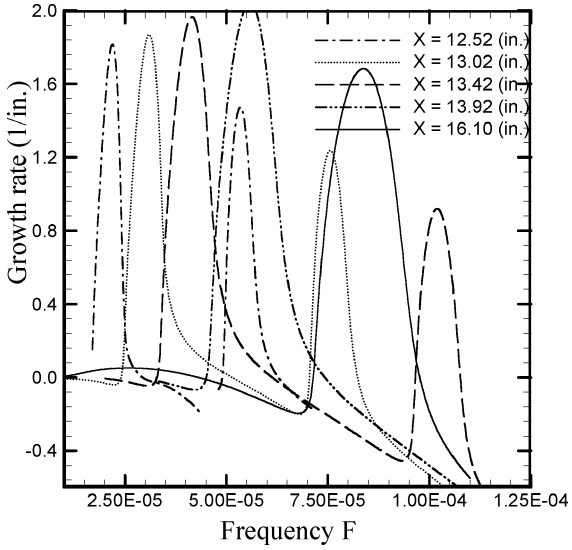

Fig. 9b Growth rate from linear stability computations at different X stations (downstream of the corner).

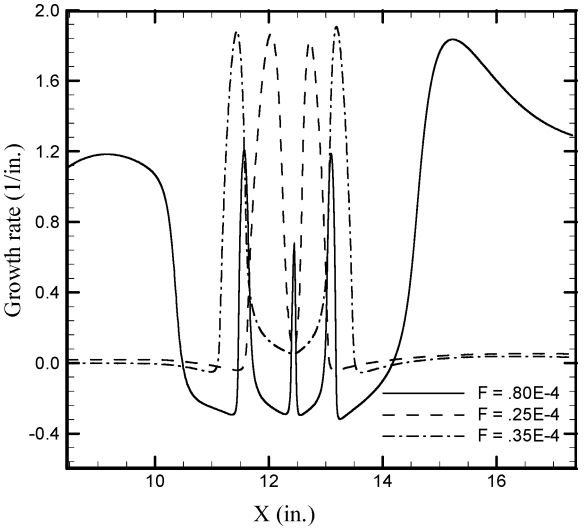

Fig. 10 Variation of growth rate for fixed frequencies in the X direction.

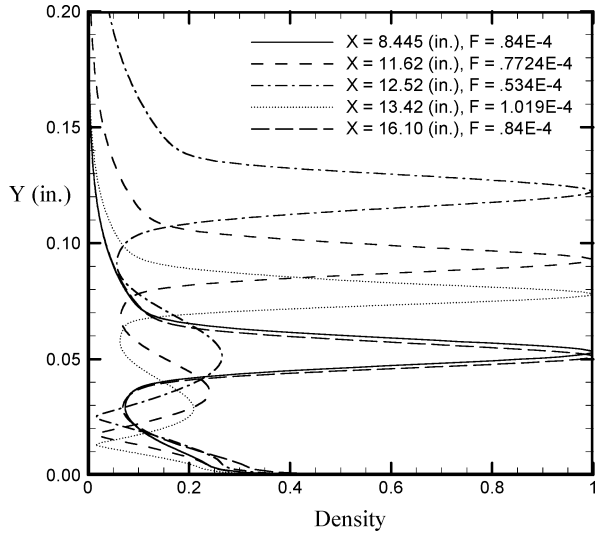

Fig. 11 Eigenfunction distribution for density at different X stations at the maximum growth rate for high frequencies.

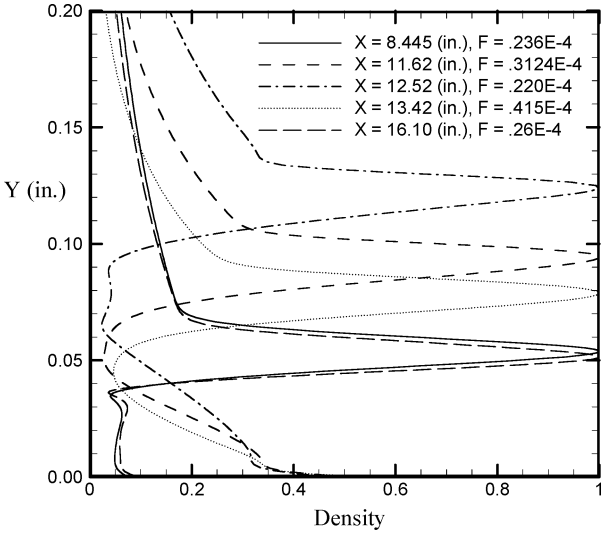

Fig. 12 Eigenfunction distribution for density at different X stations at the maximum growth rate for low frequencies.

high-frequency disturbances $F = 0.80 \times 10^{-4}$ grow uniformly in the upstream and downstream regions of the separation. But in the separated region, these disturbances have growth only in narrow confined regions and are stable or neutral in other parts. The low-frequency disturbances $F = 0.35 \times 10^{-4}$ do not grow in the regions away from the separated region, have large growth only in isolated regions in the separated region, and are stable or neutral in other parts. Hence, no disturbances have sustained growth over the entire separated region. Therefore, for these flow parameters the flow is quite stable in the separated region, and transition can only occur downstream of the separated region because of the second mode.

Figures 11 and 12 show the eigenfunction distributions for the density at the maximum growth rates at different stations $X = 8.445$, 11.52, 12.52, 13.42, and 16.10 in. Figure 11 shows the results for high frequencies, whereas Fig. 12 is for low frequencies. At stations $X = 8.445$ and 16.10 in., the calculations clearly show the classical eigenfunction distributions for the second and the first modes at the high and low frequencies. The eigenfunction for the second mode has one peak near the critical layer and has another layer near the wall. At the other X stations at the low frequencies, the same eigenfunction distributions with one peak near the critical layer and another layer near the wall are obtained. Hence, these low-frequency disturbances in the separated region belong to the

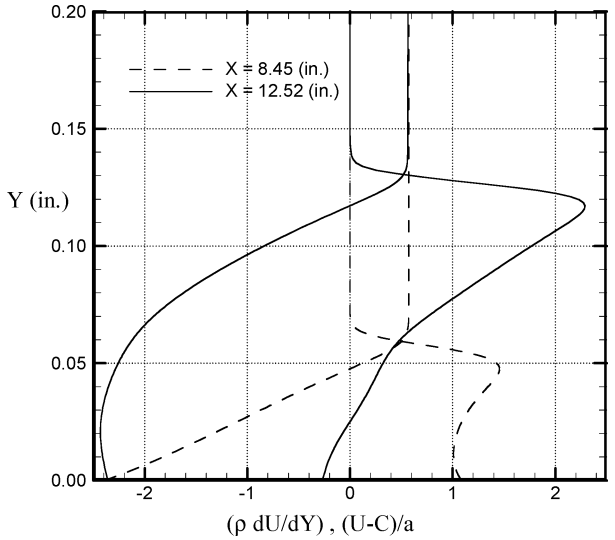

Fig. 13 Variation of $(\rho\, dU/dY)$ and the local Mach number with respect to the critical speed.

second-mode-type instability waves, but at the high frequencies the layer near the wall exhibits two maxima in the distribution. These eigenfunction distributions are similar to that for the third-mode-type instability waves.[13] To investigate this further, the distribution of two important boundary-layer functions $[\rho(dU/dY)]$ and the local Mach number relative to the mean velocity at the critical point $M_{\text{local}} = (U - C_{\text{cr}})/\sqrt{\gamma RT}$ are evaluated and plotted in Fig. 13. The results are presented for two stations at $X = 8.445$ and 12.52 in. As expected, the $[\rho(dU/dY)]$ peaks near the edge of the boundary layer and the phase speed of the disturbances are about 0.90 times the freestream velocity. The interesting observation is the width of the relative supersonic region near the wall, which is the cause for the appearance of higher acoustic modes in hypersonic boundary layers. Because the relative supersonic region is very thick for the boundary layers in the separated region, multiple high-frequency acoustic modes (second, third, etc.) could be generated in this region. Because of the thick relative supersonic region, the wavelength of the first higher mode or the second mode becomes long, and the corresponding frequency becomes lower in the separated region than in the regions away from it. Hence, the low-frequency higher modes that were just discussed $F = 0.20 \sim 0.35 \times 10^{-4}$ are the classical second modes, and the high-frequency modes $F = 0.7 \sim 1.0 \times 10^{-4}$ become the third modes in the separated region. This also explains the reason for the appearance of the multiple oscillations near the wall in the high-frequency eigenfunction distribution in the separated region. Because away from the corner the relative supersonic region narrows, the wavelengths of the higher acoustic modes become shorter, and the frequencies of these modes shift to higher values as they were observed in Figs. 9a and 9b.

C. Evolution of Second Mode over the Compression Corner

Figures 14–18 show the simulation results for the evolution of second-mode disturbances over the compression corner. The computations are performed with a small initial amplitude of $\varepsilon = 0.0001$ at several nondimensional frequencies $F = 0.85$, 0.80, 0.75, 0.65×10^{-4}. Figure 14 shows the maximum density fluctuations for the frequency $F = 0.80 \times 10^{-4}$ at a fixed time. The magnified results up to $X = 15.0$ in. are shown in the upper corner to elucidate the evolution of disturbances across the separated region. Figure 15 shows the variation of the amplitude of the maximum density fluctuations at different frequencies $F = 0.85$, 0.80, 0.75, 0.65×10^{-4}. The results clearly show that the disturbances grow exponentially upstream and downstream of the separated region but remain neutral in the separated region. This implies that the mixing layer above the separation bubble is neutrally stable for the second-mode-type disturbances. This agrees with the previous conclusions from the linear stability computations that the high-frequency

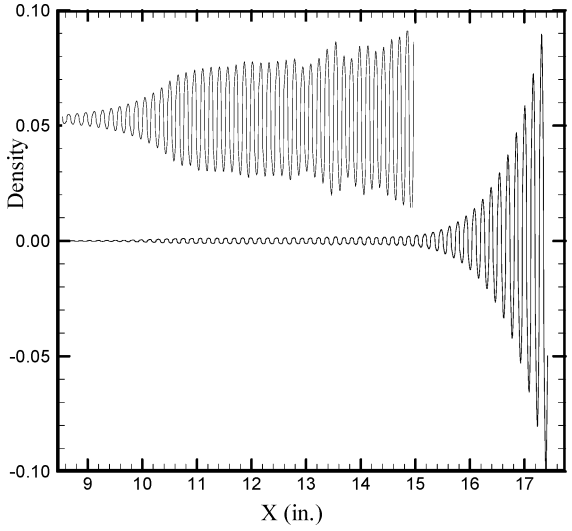

Fig. 14 Maximum density fluctuations $F = 0.80 \times 10^{-4}$. Expanded view is shown in the upper-left-hand corner.

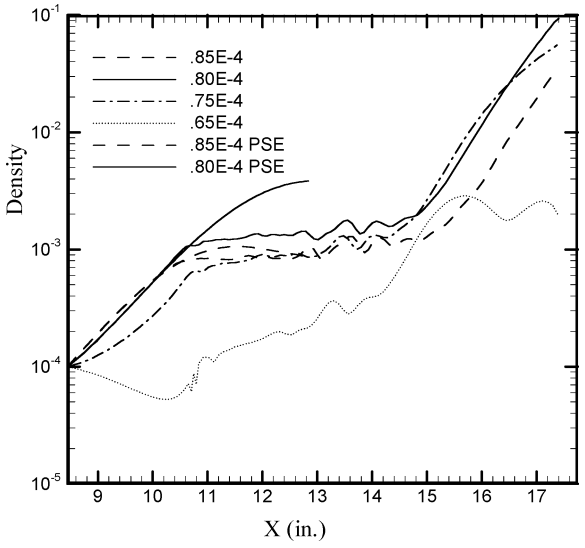

Fig. 15 Maximum amplitude of the density fluctuations at different frequencies $F = 0.85$, 0.80, 0.75, and 0.60×10^{-4}.

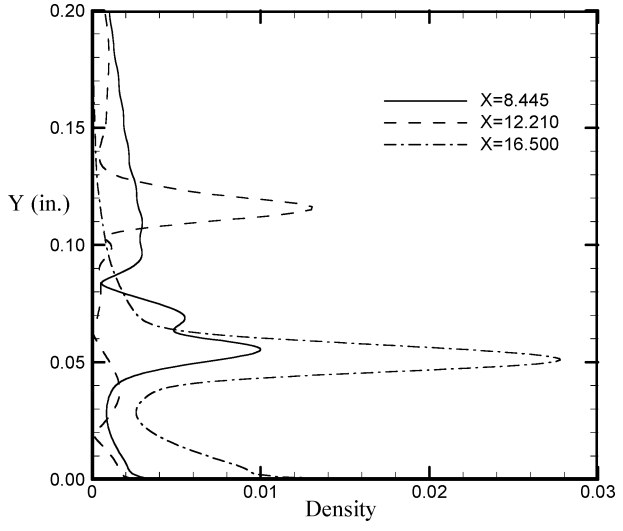

Fig. 16 Eigenfunction distribution at different axial stations for $F = 0.80 \times 10^{-4}$.

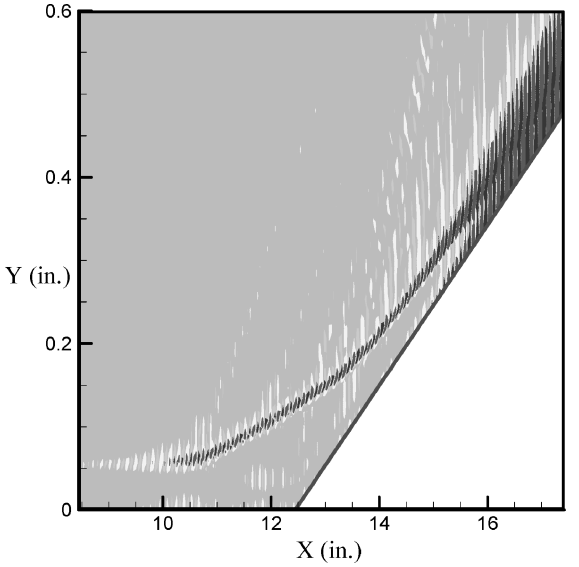

Fig. 17 Expanded view of the contours of the density fluctuations near the surface $F = 0.80 \times 10^{-4}$.

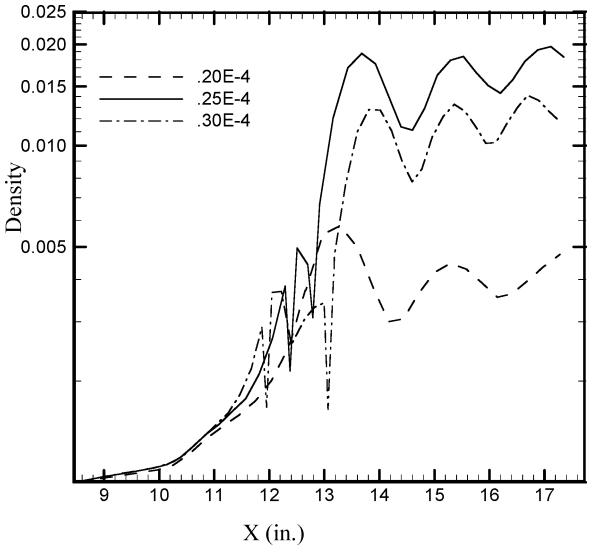

Fig. 18 Maximum amplitude of the density fluctuations at different frequencies $F = 0.20$, 0.25, and 0.30×10^{-4}.

disturbances are neutral in the separated region. Figure 15 also depicts the amplitude of the maximum density fluctuations for a flat-plate boundary layer, computed using the PSE for the nondimensional frequencies $F = 0.80 \times 10^{-4}$ and 0.85×10^{-4}. It is seen that, up to the separation point, amplitude growth for the flat plate and in the flat-plate region in the corner flow agree very well. This implies that the effect of the separation influences only downstream of the separation point. The total amplification from upstream of the computational domain $X = 8.445$ in. to downstream of the computational domain $X = 17.445$ in. is about 1000 for the most amplified frequency $F = 0.80 \times 10^{-4}$, which is equivalent to an N-factor of 7. The mean density increases by about 1.7 times across the corner because of compression. Hence, the density fluctuations based on the local boundary-layer edge density will be 1.7 times smaller than those based on the freestream value. Therefore, the amplification ratio respect to the boundary-layer edge values is smaller than 1000.

Figure 16 shows the eigenfunction distribution of the amplitude of the density fluctuations at different axial locations $X = 8.445$, 12.21, and 16.50 in. The amplitudes at $X = 8.445$ and 12.21 in. are multiplied by 100 and 10 times, respectively. The eigenfunction at $X = 8.445$ is the input to the numerical simulation and is obtained

from the PSE computations. The eigenfunction at $X = 12.21$ shows the amplitude distribution in the center of the separated region, and the eigenfunction at $X = 16.50$ shows the amplitude distribution downstream of the separated region. It is seen that the fluctuations in the separated region are confined to the outer part of the shear layer and remain small inside. The eigenfunction close to the wall in the separated region also exhibits multiple peaks in its distribution. This agrees with the linear stability results that these disturbances are the high-frequency third acoustic modes. The conclusion is that the second-mode disturbances, which enter the boundary layer upstream, become the third acoustic mode disturbances when they propagate across the separated region, and downstream, these third-mode disturbances change back into second mode.

Figure 17 shows the expanded view of the contours of the density fluctuations inside the boundary layer. The first observation is that the second-mode disturbances, as are well known, reside near the edge of the boundary layer where the critical layer is located. Another important observation is that when the disturbances evolve over the separated region they turn and follow the boundary-layer edge as neutral disturbances and do not interfere or penetrate the separation bubble region. The fluctuations inside the separation bubble are small, as was evident from the eigenfunction distribution in Fig. 16 and from the contour plot in Fig. 17.

Similarly, Fig. 18 gives the results for the evolution of low-frequency disturbances. The computations are performed with a small initial amplitude of $\varepsilon = 0.001$ at different nondimensional frequencies $F = 0.20$, 0.25, and 0.30×10^{-4}. Figure 18 shows the amplitude of the maximum density fluctuations at different frequencies. It is seen that the disturbances are almost neutral upstream and downstream of the separated region but grow exponentially only in the separated region. This agrees with the conclusion from the linear stability computations that the low-frequency disturbances grow only in isolated regions across the separated region. The total amplification from upstream of the separation, $X = 10.0$ in., to downstream of the separation, $X = 14.0$ in., is about 20 for the most amplified frequency $F = 0.25 \times 10^{-4}$. As in the high-frequency case, the instability waves do not penetrate the separation bubble and remain confined in the mixing layer above the separation bubble.

IV. Conclusions

This study investigates numerically the stability of hypersonic boundary layers over a compression corner. Unsteady three-dimensional compressible N-S equations in generalized coordinates are solved using a fifth-order WENO scheme for spatial discretization and a third-order TVD scheme for time integration. The mean flow and the evolution of high-frequency second-mode disturbances are computed for a hypersonic flow over a 5.5-deg compression corner. The mean-flow computations agree with the earlier findings that, because of the strong shock, the boundary layer separates upstream of the corner and two compression waves form near the separation and reattachment points. The boundary layer grows steeply like a wedge until the middle part of the separated region and shrinks again in a short distance near the reattachment region. The linear stability results show that, in the regions upstream and downstream of the separated region, the high-frequency second mode is unstable. In the separated region, multiple unstable modes appear as a result of the thick relative supersonic region near the wall. Because of this thick supersonic region, the frequency of the first higher mode, that is, the second mode, is lower than what is outside of the separation region. However, these higher modes have large growth rates only in isolated narrow regions and do not have a sustained growth over the separated region.

The evolution of the second-mode disturbances, computed using the direct numerical simulation, shows that the disturbances grow exponentially upstream and downstream of the separated region but remain neutral across the separated region. The computations also identified the high-frequency disturbances that enter upstream of the separated region as the second-mode type become the third mode when they propagate across the separated region, and this third mode transforms back to second mode as they evolve downstream. Similarly, the low-frequency disturbances that are the first mode type away from the separated region become the second mode in the separated region. These low-frequency disturbances grow only across the separated region and remain almost neutral away from it. There are no two-dimensional disturbances that grow uniformly in the entire domain. Hence, for the flow parameters investigated, the transition cannot occur on the separation bubble because of the second mode, and transition will only happen downstream of the separated region because of the second mode. The maximum N-factor up to the second corner region is about seven, and this occurs for a disturbance with a frequency of 214 kHz. According to the experiment,[12] the transition from laminar to turbulent for this case occurred close to the second corner. Therefore, the present calculations conform to the predictions from the linear theory that the transition might not occur for this case before the second corner in quiet environments. This paper does not consider the other two effects, three-dimensionality and nonlinearity. In the transition process, they play a very important role, and in the nonlinear investigation they have to be included.

References

[1]Ackeret, J., Feldmann, F., and Rott, N., "Investigation of Compression Shocks and Boundary Layers in Gases Moving at High Speed," NACA TM-1113, Jan. 1947.

[2]Lewis, J. E., Kubota, T., and Lees, L., "Experimental Investigation of Supersonic Laminar, Two-Dimensional Boundary Layer Separation in a Compression Corner with and Without Cooling," *AIAA Journal*, Vol. 6, No. 1, 1968, pp. 7–14.

[3]Inger, G. R., "Similitude Properties of High-Speed Laminar and Turbulent Boundary Layer Incipient Separation," *AIAA Journal*, Vol. 15, No. 6, 1977, pp. 619–623.

[4]Rudy, D. H., Thomas, J. L., Kumar, A., Gnoffo, P. A., and Chakravarthy, S. R., "Computation of Laminar Hypersonic Compression-Corner Flows," *AIAA Journal*, Vol. 29, No. 1, 1991, pp. 1108–1113.

[5]Grasso, F., Leone, G., and Delery, J. M., "Validation Procedure for the Analysis of Shock-Wave/Boundary-Layer Interaction Problems," *AIAA Journal*, Vol. 32, No. 9, 1994, pp. 1820–1827.

[6]Simeonides, G., Hasse, W., and Manna, M., "Experimental, Analytical, and Computational Methods Applied to Hypersonic Compression Ramp Flows," *AIAA Journal,* Vol. 32, No. 2, 1994, pp. 301–310.

[7]de Luca, L., Cardone, G., Aymer de la Chevalerie, D., and Fonteneau, A., "Viscous Interaction Phenomena in Hypersonic Wedge Flow," *AIAA Journal*, Vol. 33, No. 12, 1995, pp. 2293–2298.

[8]Chapman, D. R., Kuehn, D. M., and Larson, H. K., "Investigation of Separated Flows in Supersonic and Subsonic Streams with Emphasis on the Effects of Transition," NACA TN-3869, March 1957.

[9]Lighthill, M. J., "On Boundary Layers and Upstream Influence. I. A Comparison Between Subsonic and Supersonic Flows," *Proceedings of the Royal Society of London, Series A*, Vol. 217, No. 1129, 1953, pp. 344–357.

[10]Lighthill, M. J., "On Boundary Layers and Upstream Influence. II. Supersonic Flows Without Separation," *Proceedings of the Royal Society of London, Series A*, Vol. 217, No. 1131, 1953, pp. 478–507.

[11]Stewartson, K., and Williams, P. G., "Self-Induced Separation," *Proceedings of the Royal Society of London, Series A*, Vol. 312, No. 1508, 1969, pp. 181–206.

[12]Berry, S. A., DiFulvio, M., and Kowalkowski, M. K., "Forced Boundary Layer Transition on X-43 (Hyper-X) in NASA LaRC 20-Inch Mach 6 Air Tunnel," NASA TM-2000-210316, Aug. 2000.

[13]Mack, L., "Boundary Layer Stability Theory," Jet Propulsion Lab., Rept. 900-277, Pasadena, CA, Nov. 1969.

[14]Balakumar, P., Zhao, H., and Atkins, H. L., "Stability of Hypersonic Boundary Layers over a Compression Corner," AIAA Paper 2002-2848, June 2002.

[15]Shu, Chi-Wang, "Essentially Non-Oscillatory and Weighted Essentially Non-Oscillatory Schemes for Hyperbolic Conservation Laws," NASA CR-97-206253, ICASE Rept. 97-65, Hampton, VA, Nov. 1997.

[16]Atkins, H. L., "High-Order ENO Methods for the Unsteady Compressible Navier–Stokes Equations," AIAA Paper 91-1557, June 1991.

[17]Herbert, T., "Parabolized Stability Equations," *Annual Review of Fluid Mechanics*, Vol. 29, 1997, pp. 245–283.

H. Reed
Associate Editor